Optical Properties of Single Plasmonic Holes Probed with Local Electron Beam Excitation

Toon Coenen and Albert Polman*

Center for Nanophotonics, FOM Institute AMOLF, Science Park 104, 1098XG Amsterdam, The Netherlands

ABSTRACT Similar to nanoparticles, nanoscale holes form a basic building block in a wide array of nanophotonic devices. Here we study the spectral and angular cathodoluminescence response of individual nanoholes with diameters ranging from 50 to 180 nm. Taking advantage of the deep-subwavelength excitation resolution, we find that the holes can be excited efficiently at the edge of the hole and that the response becomes stronger in the near-infrared part of the spectrum for larger holes. Using finite-difference time-domain simulations, we characterize the resonant modes inside the holes. We measure the angle-resolved cathodoluminescence response and observe strong beaming toward the side of electron beam excitation, complementary to what was shown for nanoparticles. The angular response can be explained by assuming a coherent superposition of radiating dipole moments, where the contribution of in-plane magnetic and electric dipole components increases for larger diameters.

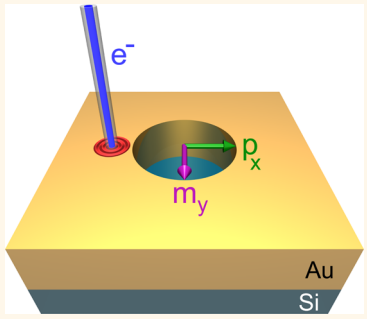

KEYWORDS: plasmonic apertures · nanoholes · cathodoluminescence spectroscopy · electron beam · directionality · magnetic/electric dipole emission

Nanoscale apertures in a metal film form a key basic building block for plasmonic devices.[1] Similar to nanoparticles, nanoscale holes and slits have the ability to strongly confine light due to localized plasmon resonances that are supported by the structure, which for example allows strong enhancement of fluorescence.[2] Since a hole is the geometrical inverse of a nanoparticle its transmission and reflection properties are complementary to that of a particle (Babinet's principle,[1,3−7] strictly speaking this only holds for 2D structures in a perfectly conducting film[8]). Furthermore, subwavelength holes diffract light in quasi-cylindrical waves (QCWs) and can couple to bound surface plasmon polaritons (SPPs) in plasmonic films which provide extra channels through which holes can be excited and coupled.[9−13] These coupling mechanisms have been utilized in ordered arrays to obtain extraordinary transmission[1,14] and absorption,[15] where the transmission/absorption cross section exceeds the geometrical cross section of the holes. Due to their accessible open geometry and unique transmission and absorption characteristics, plasmonic holes may find applications in CMOS cameras as color filters,[16,17] optical data storage,[18] and nanoscale sensors.[19−21]

Although the collective optical properties of holes in arrays have been studied extensively, characterization of individual holes is difficult owing to their subwavelength size. It has been demonstrated that by using scanning near-field microscopy[12,22] and scanning tunneling microscopy,[23] fundamental scattering properties can be measured. Alternatively, experimental techniques that employ a fast electron beam as excitation source, like electron energy-loss spectroscopy (EELS) and cathodoluminescence (CL) spectroscopy, have been used to reveal the resonant properties of circular holes,[24] rectangular holes,[25] nanoslits,[6,7] and inverse split rings.[26] In this article, we aim to further elucidate the local optical response of individual deep-subwavelength plasmonic holes, by using angle-resolved CL imaging spectroscopy (ARCIS).

RESULTS AND DISCUSSION

Sample. We used focused-ion-beam (FIB) milling to pattern circular holes in a gold film on a silicon interface, with diameters D ranging from 50 to 180 nm in steps of 5 nm and a depth of 80 nm (we stop the milling process at the silicon interface). Electron micrographs of the resulting structures are shown as insets in Figure 1a. Inherent to the

* Address correspondence to polman@amolf.nl.

Received for review May 6, 2014 and accepted June 17, 2014.

Published online June 17, 2014
10.1021/nn502469r

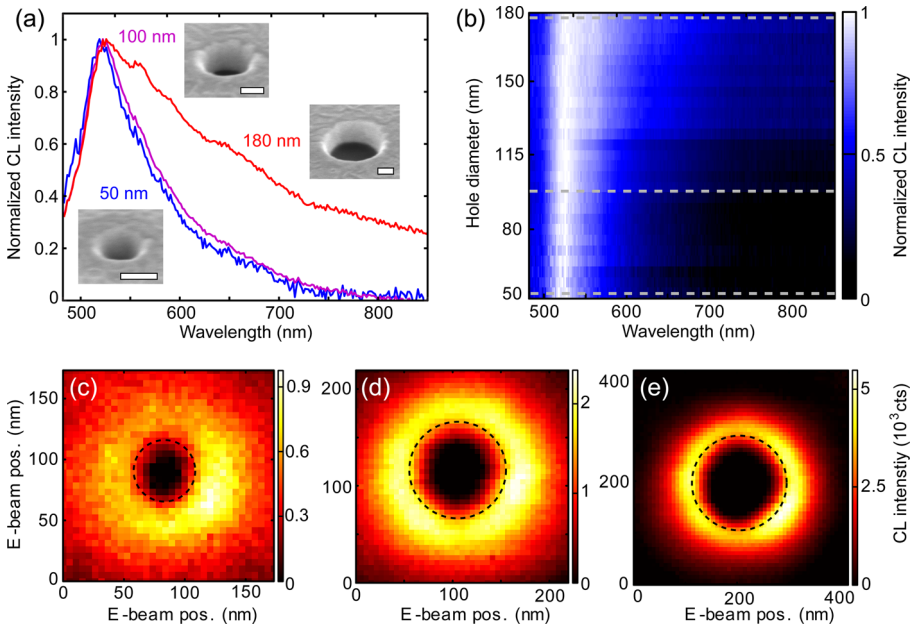

Figure 1. (a) Spatially integrated normalized CL spectra for Au nanoholes with D = 50, 100, and 180 nm. Scanning electron micrographs of the corresponding holes are shown as insets in which the scale bars represent 50 nm. The images were taken at a 52° sample tilt. (b) Integrated peak-normalized CL spectra for a range of different nanohole diameters in 5 nm steps. The gray dashed lines indicate diameters for which spectra are shown in (a). CL intensity as a function of excitation position for (c) D = 50 nm, (d) D = 100 nm, and (e) D = 180 nm at λ_0 = 520 nm, integrated over a 20 nm bandwidth. The black dashed circles indicate the edge of the hole.

FIB milling process, there is some tapering of the hole due to material redeposition. The lowest-order propagating mode in a circular hole is cut off for wavelengths larger than the cutoff wavelength; $\lambda_{cutoff} \approx 1.7D$,[1] which for D = 180 nm holes, corresponds to λ_{cutoff} = 306 nm. Therefore, we expect that the fundamental waveguide mode is cut off in the visible/near-infrared (NIR) regime for the holes that are considered in this experiment. The transmission through an 80 nm thick gold film is <5% for this wavelength range as calculated by an analytical Fresnel code, so any direct transmission through the gold film is strongly attenuated.

Spectral Response. We first measure the local spectral response of the holes. To that end, we raster scan the electron beam (30 keV acceleration voltage, 0.8 nA current, 5−10 nm beam diameter) in 5 nm steps for $D \leq 100$ and 10 nm steps for $D > 100$ nm and collect the resulting cathodoluminescence emission using a paraboloid mirror after which the spectrum is measured with a spectrometer. We use an integration time of 1 s per pixel. Figure 1a shows the spatially averaged spectrum for D = 50, 100, and 180 nm holes, respectively. The spectra are corrected by subtracting the transition radiation (TR) from an unstructured part of the gold film and multiplying with the system response. In principle, the phase of the TR with respect the hole scattering should also be taken into account when doing the background subtraction, but this is not possible as we can only measure intensities in our setup. However, to first order, this subtraction still approximately corrects the DC offset in the CL signal due to the TR, allowing us to better isolate the CL signal from the hole. The system response was calibrated using the measured TR radiation in combination with the theoretically calculated spectrum.[27] Because the signal within the hole is lower than the TR background, we get negative intensity values inside the hole, so we mask this area to obtain the integrated spectrum such that it does not artificially perturb the spectrum. For D = 50 nm and D = 100 nm holes, we observe a relatively narrow peak centered around λ_0 = 520 nm. For D = 180 nm, the peak wavelength is also around 520 nm and a long tail extending into the NIR regime is observed. Because this hole is significantly larger in size, a stronger response in the red/NIR part of the spectrum can be expected. Figure 1b shows the spatially integrated CL intensity as a function of wavelength for all studied hole diameters in which we can clearly see the gradual broadening of the response for larger diameters.

It is also insightful to study the spatial excitation profiles of the holes. Figure 1c−e shows the spatial distributions at λ_0 = 520 nm. For all diameters, we observe a bright ring around the hole, whereas the hole itself remains dark. For excitation in the center of the hole, the evanescent electron fields cannot polarize the metal because the edges are too far away, so efficient driving of a p_z component in the center is not possible like is the case for nanoparticles of similar dimensions.[28] Furthermore, any radiation that is generated at the silicon interface or in the silicon bulk

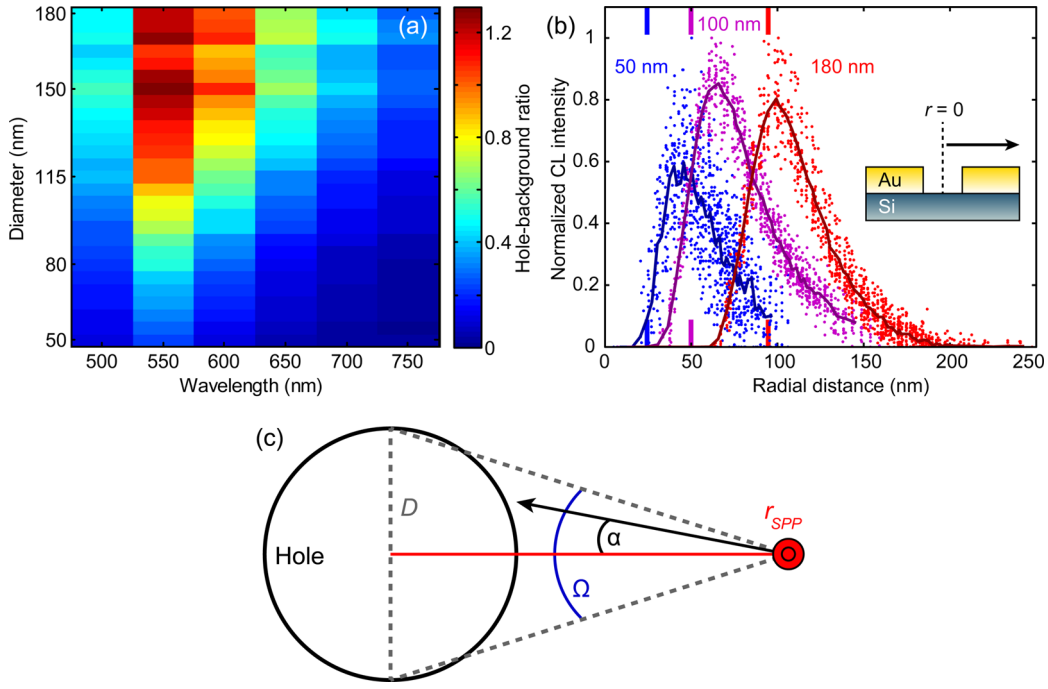

Figure 2. (a) Hole signal to TR background ratio for different hole diameters and wavelengths integrated over a 50 nm bandwidth. The color map represents $(I_{tot} - I_{TR})/I_{TR}$. (b) Radial dependence of CL signal from the hole at $\lambda_0 = 520$ nm (averaged over a bandwidth of 20 nm) for $D = 50$ nm (blue), $D = 100$ nm (magenta), and $D = 180$ nm (red). Each dot represents a CL pixel to which we assign a radial distance from the hole center. The solid curves represent the average value of 20 binned data points. (c) Schematic representation of the interaction of a circular SPP wave excited at position r_{SPP} with a hole. The geometrical parameters used in the model are indicated in the figure.

cannot efficiently couple to free-space radiation into the upper angular hemisphere because the waveguide mode in the hole is beyond cutoff for these diameters. Similar spatial excitation profiles were observed in the EELS measurements in ref 24, although those were measured on a free-standing silver film. We note that the larger holes are significantly brighter than the smaller holes. This is quantified in Figure 2a, where we compare the maximum signal strength at the hole $I_{tot}(\lambda_0)$ with the constant TR background $I_{TR}(\lambda_0)$ by plotting $(I_{tot} - I_{TR})/I_{TR}$ for different diameters and wavelengths. Such a trend is expected as larger holes scatter more efficiently into the far field.

To better understand the excitation processes that are involved in the CL experiment, we study the decay of the CL signal away from the hole. This is visualized in Figure 2b, where we plot the CL intensity (with the TR background subtracted) as a function of the radial distance from the hole center at $\lambda_0 = 520$ nm, extracted from the images shown in Figure 1c–e. The signal decays rapidly away from the hole edge. The $1/e$ distance corresponds to ~35 nm for each hole diameter. Within this spatial region, we expect that there is direct coupling to the near-field of the hole resonance. Because of the surrounding gold film, indirect excitation of the holes is also possible through SPPs that are generated by the electron beam away from the hole and subsequently scattered out by the hole.

The interaction with such a circular SPP wave would rapidly decay as a function of distance to the hole. We estimate this decay length with a simple intuitive model of which the relevant parameters are sketched in Figure 2c. First, the degree of interaction of the hole with the SPP wave drops as the electron beam moves away further from the hole due to the decreasing 2D acceptance angle ($\Omega = \tan^{-1}(D/2r_{SPP})/\pi$) covered by the hole. Here r_{SPP} is the position at which the SPP wave is generated (at the beam impact position) relative to the hole center. For this simple calculation, we neglect any effects of hole shape and assume that the effective scattering cross section equals the hole diameter.

Second, we take into account Ohmic loss, as the SPP wave propagates toward the hole. In order to quantify the propagation losses, we calculate the dispersion characteristics of the SPPs in our layered system using an analytical mode solver. We find that the layer supports two plasmon modes, which exhibit dispersion very similar to the single interface plasmon modes for a vacuum–gold and silicon–gold interface, respectively, indicating that there is little coupling between the top and bottom interface of the gold film. The guided plasmon mode on the silicon–gold interface is heavily damped and will couple poorly to free space radiation in the upper angular hemisphere as it has to couple out through the hole. Hence we expect that the CL response is dominated by SPPs from the top interface. We find that the propagation length

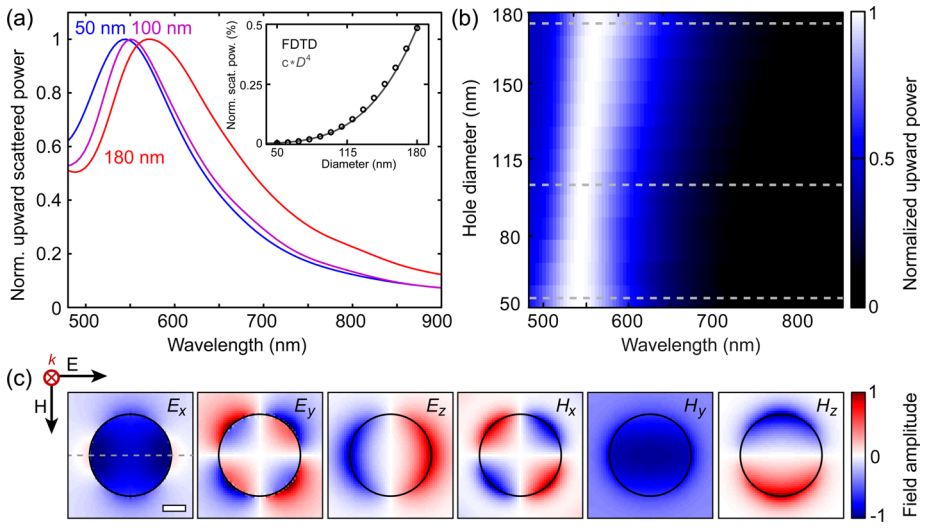

Figure 3. (a) Upward scattering for D = 50, 100, and 180 nm holes for plane-wave excitation under normal incidence, calculated using a TFSF simulation in FDTD. We only plot the part of the light that is emitted upward as that is the part that is collected in our CL system. The spectra have been normalized to 1 for visibility as the largest hole scatters much more strongly than the smallest one. The inset shows the amount of upward scattered power relative to the incoming power as a function of diameter (black circles), integrated over the full spectral range. Through the data, we have fitted a D^4 curve (gray curve) scaled with an arbitrary constant c. (b) Simulated peak-normalized plane-wave spectra for a range of different nanohole diameters in 5 nm steps. The gray dashed lines indicate diameters for which spectra are shown in (a). (c) In-plane field (xy) cuts for D = 180 nm at λ_0 = 575 nm showing the real part of E_x, E_y, E_z, H_x, H_y, and H_z. The cuts are taken at half-height, 40 nm above the substrate. For reference, we have included the incoming plane-wave polarization. The scale bar is 50 nm.

L_{SPP} calculated from Im$\{k_{SPP}\}$ for this mode is larger than 350 nm in the spectral region of interest. Its effect on the overall signal decay hence is relatively small compared to the acceptance angle losses.

To obtain the correct SPP propagation decay, in principle, we have to take into account the angle-dependent propagation distances to the hole, which leads to a exp $(-r_{SPP}/L_{SPP}\cos(\alpha))$ term for the propagation loss[29] (α is the angle with respect to the axis that is defined by the electron beam position and the hole center; see Figure 2c). For small acceptance angles, $\alpha \simeq 0$ and the SPP decay reduces to exp $(-r_{SPP}/L_{SPP})$.

Using the model described above, we find effective decay lengths from the hole edge (for λ_0 = 520 nm) for D = 50, 100, and 180 nm hole diameters of 51, 90, and 140 nm, respectively. However, in the experiment, we do not observe a noticeable diameter dependence in the CL signal decay, and the decay occurs over significantly shorter distances (see Figure 2b). This indicates that direct near-field coupling rather than indirect outcoupling of SPPs dominates the CL experiment.

Simulation Results. To gain more insight into the resonant properties of these holes, we perform finite-difference time-domain simulations (FDTD).[30] In particular, we use a total-field scattered-field source to calculate the scattering spectra for hole diameters between 50 and 180 nm (in 10 nm steps) under plane-wave illumination at normal incidence. Figure 3a shows the normalized upward scattered power spectrum for the same diameters as in Figure 1a. Similar to the experiment, we only consider the upward scattered power. We note that the total scattered power spectrum (not shown here) looks very similar to the upward scattered power, indicating that upward scattered power is representative for the overall scattering response.

Figure 3b shows the evolution of the spectrum in the range D = 50−180 nm (calculated in 10 nm steps). The scattering spectrum only changes moderately with diameter, similar to what is observed in the CL experiment. However, some red shifting occurs as is expected for such resonant modes which is not observed in the CL data. We attribute this to the fact that besides exciting in-plane modes, like is the case for the plane-wave excitation simulations in FDTD, the electron beam can also couple to vertically polarized modes. In particular, the electron beam can couple to a vertically polarized mode at the hole edge which should not shift significantly with diameter as it is mainly influenced by the metal thickness. As a result, the peak emission remains at the same position, but the in-plane response increases and red shifts with diameter, leading to the observed line shapes in Figure 1a,b.

We further note that the normalized scattering cross sections Q_{scat} (normalized to the hole area) are quite low (Q_{scat} = 1.1 for D = 180 nm at the peak wavelength of 575 nm) compared to those for nanoparticles. This could be related to the fact that a hole has less polarizable metal available for a given geometrical cross section. In the inset of Figure 3a, we show the amount of upward scattered power integrated over the full spectrum for different hole diameters,

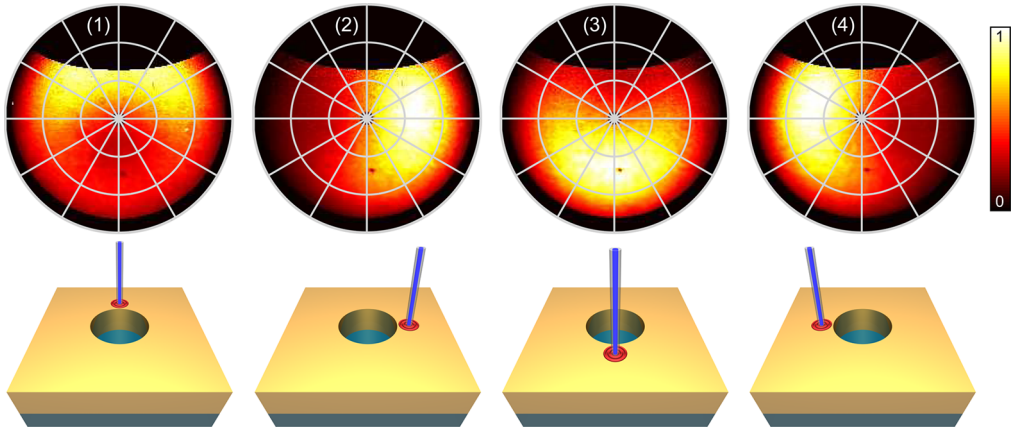

Figure 4. Experimental normalized angular cathodoluminescence emission patterns collected from a 100 nm diameter nanohole at λ_0 = 500 nm for excitation ~20 nm from the edge for four orthogonal azimuthal angles: (1) 0° (top), (2) 90° (right), (3) 180° (bottom), and (4) 270° (left). In the angular patterns, the three concentric circles represent zenithal angles θ = 30°, 60°, and 90°, respectively. The excitation positions are indicated by the schematics below the patterns. The patterns have been normalized to the maximum intensity value for all four patterns to show the relative brightness for different excitation positions.

normalized to the incident power in the simulation. We observe a D^4 increase in the amount of scattered power for increasing hole diameter. This is consistent with the notion that the emitted power for dipoles is proportional to the square of the polarizability, which itself generally scales with volume. In this case, the effective hole volume increases by D^2 for increasing diameter leading to a D^4 overall power dependence.

By studying the induced near-field distributions, one can identify the nature of the resonant peak. Figure 3 shows all six electric and magnetic field components for an in-plane cut at half-height (40 nm above the silicon substrate for D = 180 nm at λ_0 = 575 nm). The electric and magnetic fields show a mix of in-plane electric and magnetic dipole contributions. The fields are consistent with a p_x electric dipole moment and m_y magnetic dipole moment, commensurate with the incoming plane-wave electric and magnetic field polarizations. Furthermore, it is clear that there is a significant E_z contribution near the edge of the hole, which is the electromagnetic field component to which the electron beam couples efficiently. The dipole modes we observe here are infinitely degenerate due to the circular symmetry of the hole, which is why we observe a bright ring in the excitation maps in Figure 1c–e, rather than the E_z profile calculated with FDTD which shows two hotspots along the polarization direction. The 1/e decay value for $|E_z|^2$ is ~20 nm away from the hole edge where the field is maximum, which is slightly shorter than the experimental values obtained with CL (see Figure 2b). Possibly, this is related to the fact that in the FDTD we consider a perfectly cylindrical hole, whereas in the experiment, the intensity profile is constructed with a rounded shape at the edge. The field maps were also calculated for the other diameters and free-space wavelengths and show similar patterns to Figure 3c.

Angular Response. Next, we study the angular emission distribution of the holes when excited by an electron beam. It has been shown that holes/slits surrounded by grating-like corrugations can acts as highly directional emitters of free space light[31] or SPPs[32] which can be used to enhance and direct fluorescence originating from the hole, for instance.[33,34] Even unstructured holes/slits can act as directional emitters owing to the fact that they support electric and magnetic dipole modes that can interfere in the far field (Kerker effect).[22,35,36] To study the directionality of holes, we measure the angular emission pattern using ARCIS. We collect angular patterns while exciting a single hole at four orthogonal edge positions (left, right, top, and bottom) for center wavelengths λ_0 = 400–750 nm in 50 nm steps using band-pass filters (40 nm bandwidth). For these edge excitation measurements, we position the electron beam ~20 nm from the hole edge. We do not collect an angular pattern for excitation at the center of the hole as there is practically no CL emission at that position. For the angular patterns, we cannot subtract the background radiation pattern from a bare gold substrate which corresponds to a symmetric torus,[37] as that leads to negative emission values for certain angles.

Figure 4 shows angular patterns for a D = 100 nm hole measured for top (1), right (2), bottom (3), and left (4) edge excitation as indicated by the schematics below the angular patterns. Similar to what we found for the complementary nanoparticle geometry,[28] the angular pattern corotates with the excitation position. This implies that a different combination of multipole components is excited at each position. Light is scattered toward the direction of the excitation point, which is opposite to what was observed for the nanoparticles,[28] illustrating the complementarity between the two geometries. The backward-to-forward scattering ratio calculated by dividing the integrated

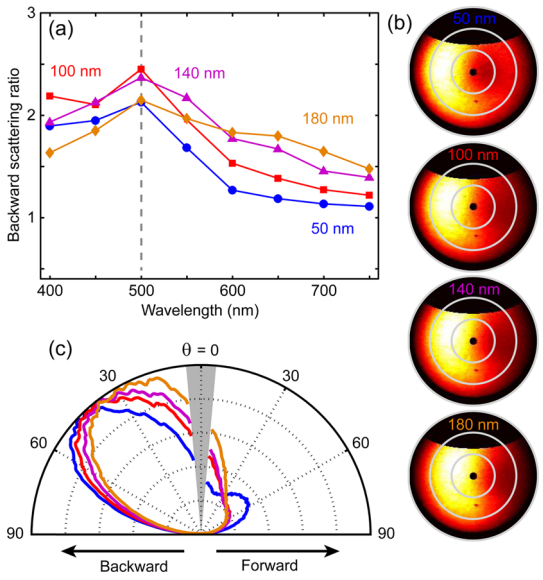

Figure 5. (a) Backward-to-forward scattering ratio as function wavelength for different hole diameters. The data were averaged over two excitation positions (left and right). (b) Angular patterns for D = 50, 100, 140, and 180 nm at λ_0 = 500 nm, as indicated by the gray dashed line in (a). (c) Cross cuts through radiation patterns in (b), plotted with the same color code as in (a). The cross cuts have been integrated over a range of ϕ (ϕ = 60−120° and ϕ = 240−300°). All patterns in (c) have been normalized to 1. No data are collected for the gray region which corresponds to the angular range that is taken by the hole in the parabolic mirror. The arrows indicate the backward and forward direction, respectively.

backward half of the angular hemisphere by the forward half is quantified in Figure 5a for different diameters and wavelengths. Here, backward is defined as toward the excitation position, and forward is defined as away from the excitation position. For all measurements, we observe dominant backward scattering (ratio being larger than 1), although for smaller hole diameters, the scattering ratio approaches 1 more quickly for increasing wavelength. This is to be expected as the smallest holes do not scatter efficiently in the red, leaving the azimuthally symmetric TR emission as the dominant source of radiation, as can also be seen in Figure 2a.

Contrary to what was found for the nanoparticles, varying the diameter does not have a very profound influence on the directionality. This is emphasized in Figure 5b, where we show angular patterns for D = 50, 100, 140, and 180 nm at λ_0 = 500 nm for excitation on the left edge of the hole. These angular patterns look very similar. Figure 5c shows cross cuts through the patterns in Figure 5b, integrated over a range of ϕ (60−120° and 240−300°) to improve the signal-to-noise ratio. For increasing diameter, we observe a slow but gradual shift in the pattern toward the normal, suggesting that the in-plane dipole components become more dominant.

Based on the FDTD simulations, we know that the hole supports in-plane electric and magnetic dipole modes. From the driving symmetry of the vertical-dipole-like electron beam excitation, we expect that for excitation on the left side of the hole we can excite a p_x and m_y component. Both have a significant E_z component at the electron beam impact position (also see Figure 3c in which the same modes are excited by a plane wave), allowing efficient driving by the electron beam. When we move toward the top of the hole, the excited moments would corotate and we would have a p_y and m_x component, related to the circular degeneracy of the resonant modes. Although interference between these in-plane dipole components can lead to enhanced out-of-plane upward or downward scattering,[38−41] it cannot explain the backward−forward asymmetry in our angular measurements. Such an asymmetry requires an out-of-plane dipole component as well. In our experiment, we generate TR emission at the edge of the hole which has an effective p_z dipole moment. As is clear from Figure 2a, the TR contribution is significant and can interfere with the radiation scattered by the hole, similar to what was observed for gratings.[27] Furthermore, the hole itself can also support a p_z component[8,12] due charge separation across the hole edge along the vertical direction. These two potential p_z contributions are difficult to separate in this experiment, although the spectra in Figure 1 suggest that this vertical edge mode plays a significant role in the CL signal.

Regardless of the origin of the p_z component, we expect that the resulting angular pattern is caused by coherent interference of p_z, p_x, and m_y dipole moments. As a simple estimate for the angular patterns, we can take the coherent sum of a p_z moment and in-plane components m_y and p_x where we use the ratios from Figure 2a as the ratio between the out-of-plane and in-plane components. To take into account substrate interference, we assume that the dipoles are located at a vacuum−gold interface. In our model, we place the m_y and p_x components corresponding to the hole resonance at the center of the hole, whereas the p_z component is positioned at the edge of the hole representing the TR emission/edge mode at the electron beam impact position (spaced by a distance D/2 from the hole center). It has been shown that for holes in this size range the magnetic and electric polarizabilities are very similar.[22] Hence, we assume that the m_y and p_x contributions are equal. Furthermore, we assume that there is a fixed phase relation between the dipole components. This is not necessarily true in the experiment but as we will show this assumption works quite well. In fact, if one would assume a profoundly different phase relation that would lead to clear changes in the angular patterns or even a flip from backward to forward beaming, which would be inconsistent with the experiment.

Figure 6a shows the calculated angular radiation patterns for the coherent interference between dipole moments taking the assumptions mentioned above. A top view of the dipole configuration is shown

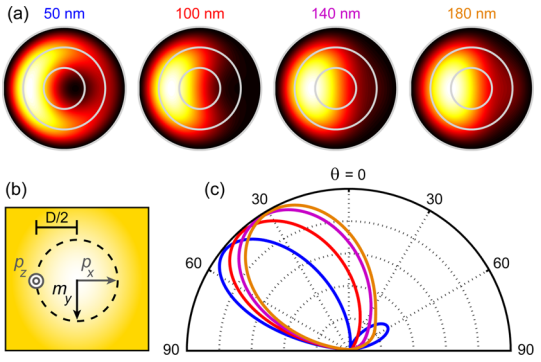

Figure 6. (a) Angular patterns for a combination of p_z, p_x, and m_y, where the ratios between in-plane and out-of-plane components for the different hole diameters are taken from Figure 2a. This combination of dipole moments is expected for excitation on the left edge of the hole. (b) Schematic top view of the dipole orientations with respect to the hole (included as circular dashed line for reference) as used in the model. We position the p_z dipole at the edge of the hole at the electron impact position. (c) Cross cuts through (a) using the same color code and integrated over the same range of ϕ as in Figure 5c.

schematically in Figure 6b. In Figure 6c, we show the cross cuts through the patterns in a similar to Figure 5c. Although this model is very simple and is based on several assumptions, it already gives remarkably good agreement with the experimental data, illustrating that the magnitude and relative phase of the dipole moments is close to what we assumed. Because the in-plane components become stronger for larger diameters, the emission lobe moves toward the normal for larger holes, going from $\theta = 50°$ to $\theta = 30°$, which matches well with the data in Figure 5c. Furthermore, for the smallest diameter, the p_z component is relatively strong which leads to a small forward lobe. This additional lobe is also visible in the CL data (see Figure 5). We note that angular emission profiles of the nanoparticles had significant quadrupolar contributions,[28] but for the holes, these do not seem to be necessary to explain the data so they are not fully complementary. This suggests that Babinet's principle does not fully apply for this hole/particle combination which we attribute to the fact that these are 3D systems consisting of gold rather than 2D structures in a perfectly conducting film.

The fact that the hole response appears to be mainly dipolar agrees well with our plane-wave simulation results and with results obtained by Rotenberg *et al.*,[12,22] even though the local electron beam driving creates stronger gradients that potentially could enhance higher order moments.[42] The far-field directionality in this experiment is complementary to the directionality that was observed in the near-field,[22] although in that case the holes were driven through SPPs which cannot efficiently drive an electric dipole moment along the propagation direction due to its transverse magnetic wave nature. Furthermore, there was no TR emission component present in those experiments, as that is unique to electron beam excitation. In the future, performing 3D full-wave simulations using the 3D boundary element method (BEM) or the discrete dipole approximation (DDA) method, which take into account both the electron beam excitation and the full hole geometry, might give further insights into the precise phase relation and relative amplitudes of the induced moments. Additionally, including full polarization sensitivity in the angular CL measurements might provide extra information with which these contributions can be separated experimentally.

CONCLUSIONS

In conclusion, we have used angle-resolved cathodoluminescence spectroscopy to unravel the local response of individual nanoscale holes patterned in a gold film at deep-subwavelength excitation resolution. We studied the influence of hole diameter on the scattering spectrum and angular radiation profile. In the spectra, we find a strong contribution around $\lambda_0 = 520$ nm for all diameters. The response in the red/NIR spectral region increases for larger diameters. By studying the decay of the CL signal away from the hole, we determine that direct coupling to the hole resonance near-fields is the main source of coupling. Using finite-difference time-domain simulations, we further elucidate the scattering behavior and deduce from the induced near-fields that the emission has both electric and magnetic dipole character. The interference of these in-plane components with an out-of-plane electric dipole moment gives rise to transverse beaming by the holes, complementary in direction to what was found for nanoparticles before, although the absence of quadrupolar contributions suggests that Babinet's principle is not fully applicable here. As the diameter increases, the in-plane dipole components become more dominant, leading to a shift in the main emission lobe toward the normal. This behavior is well-reproduced by a dipole interference model where we take the spectral measurements as input to determine the ratio between the in-plane and out-of-plane components. These insights could be used in the future to design and characterize novel plasmonic devices for sensing, plasmon sources, and optical data storage based on nanoscale plasmonic apertures.

METHODS

Fabrication. We deposited a 80 nm thick gold layer on a silicon substrate using thermal evaporation. To reduce the granularity of the film, we evaporated a 1 nm thick seed layer of germanium first.[43,44] Subsequently, we used focused-ion-beam (FIB) milling in a FEI Helios dual-beam system to pattern circular holes in the film, with diameters D ranging from 50 to 180 nm in steps of 5 nm and a depth of 80 nm (we stop the milling process at the silicon interface). To obtain the best patterning resolution, we used a low ion beam current (1.5 pA).

Experiment. The CL experiment was performed in a FEI XL-30 SFEG scanning electron micrope with an aluminum paraboloid mirror inside. The mirror alignment is performed using a specially designed piezoelectric positioning system. For spectral imaging, the CL was focused onto a fiber going to a spectrometer with liquid-nitrogen-cooled CCD array. For the angular measurements, the CL beam is projected onto a 1024 × 1024 imaging array. Emission patterns were obtained by mapping the 2D CCD image of the CL beam onto emission angle θ (zenithal angle) and ϕ (azimuthal angle) and correcting for the collected solid angle per CCD pixel. See refs 37 and 45 for more details on experimental setup.

Finite-Difference Time-Domain Simulations. We perform FDTD simulations using a commercial sofware package from Lumerical.[30] In particular, we use a total-field scattered-field source that isolates the scattering from the total field. To calculate the upward scattered power (similar to the CL experiment), we only use the top monitor which has an effective NA of 0.85. We use tabulated optical constants for silicon[46] and gold.[47] In order to calculate the total scattered power, the silicon substrate was approximated by a $n = 4$ lossless dielectric such that the light that is scattered down into the substrate is not attenuated by absorption in the silicon. In this case, we use a 3D power box that completely encloses the structure in order to capture all the scattering.

Conflict of Interest: The authors declare the following competing financial interest(s): A.P. is co-founder and co-owner of Delmic BV, a startup company that develops a commercial product based on the ARCIS cathodoluminescence system that was used in this work.

Acknowledgment. We would like to acknowledge Nir Rotenberg, Jorik van de Groep, and Ruben Maas for useful discussions. This work is part of the research program of the "Stichting voor Fundamenteel Onderzoek der Materie" (FOM), which is financially supported by the "Nederlandse organisatie voor Wetenschappelijk Onderzoek" (NWO). It is also funded by NanoNextNL, a nanotechnology program funded by the Dutch ministry of economic affairs, and the European Research Council (ERC).

REFERENCES AND NOTES

1. Garcia-Vidal, F. J.; Martin-Moreno, L.; Ebbesen, T. W.; Kuipers, L. Light Passing through Subwavelength Apertures. *Rev. Mod. Phys.* **2010**, *82*, 729–787.
2. Rigneault, H.; Capoulade, J.; Dintinger, J.; Wenger, J.; Bonod, N.; Popov, E.; Ebbesen, T. W.; Lenne, P. Enhancement of Single-Molecule Fluorescence Detection in Subwavelength Apertures. *Phys. Rev. Lett.* **2005**, *95*, 117401.
3. Balanis, C. *Antenna Theory: Analyses and Design*, 3rd ed.; John Wiley & Sons: New York, 2005.
4. Falcone, F.; Lopetegi, T.; Laso, M. A. G.; Baena, J. D.; Bonache, J.; Beruete, M.; Marques, R.; Martin, F. Babinet Principle Applied to the Design of Metasurfaces and Metamaterials. *Phys. Rev. Lett.* **2004**, *93*, 197401.
5. Zentgraf, T.; Meyrath, T. P.; Seidel, A.; Kaiser, S.; Giessen, H. Babinet's Principle for Optical Frequency Metamaterials and Nanoantennas. *Phys. Rev. B* **2007**, *76*, 033407.
6. Ögüt, B.; Vogelgesang, R.; Sigle, W.; Talebi, N.; Koch, C. T.; van Aken, P. A. Hybridized Metal Slit Eigenmodes as an Illustration of Babinet's Principle. *ACS Nano* **2011**, *5*, 6701–6706.
7. Rossouw, D.; Botton, G. A. Resonant Optical Excitations in Complementary Plasmonic Nanostructures. *Opt. Express* **2012**, *20*, 6968–6973.
8. García de Abajo, F. J. Colloquium: Light Scattering by Particle and Hole Arrays. *Rev. Mod. Phys.* **2007**, *79*, 1267–1290.
9. Gay, G.; Alloschery, O.; Viaris de Lesegno, B.; O'Dwyer, C.; Weiner, J.; Lezec, H. J. The Optical Response of Nanostructured Surfaces and the Composite Diffracted Evanescent Wavemodel. *Nat. Phys.* **2006**, *2*, 262–267.
10. Liu, H.; Lalanne, P. Microscopic Theory of the Extraordinary Optical Transmission. *Nature* **2008**, *452*, 728–731.
11. Parsons, J.; Hendry, E.; Burrows, C. P.; Auguié, B.; Sambles, J. R.; Barnes, W. L. Localized Surface-Plasmon Resonances in Periodic Nondiffracting Metallic Nanoparticle and Nanohole Arrays. *Phys. Rev. B* **2009**, *79*, 073412.
12. Rotenberg, N.; Spasenović, M.; Krijger, T. L.; le Feber, B.; García de Abajo, F. J.; Kuipers, L. Plasmon Scattering from Single Subwavelength Holes. *Phys. Rev. Lett.* **2012**, *108*, 127402.
13. van Beijnum, F.; Rétif, C.; Smiet, C. B.; Liu, H.; Lalanne, P.; van Exter, M. P. Quasi-cylindrical Wave Contribution in Experiments on Extraordinary Optical Transmission. *Nature* **2012**, *492*, 411–414.
14. Ebbesen, T. W.; Lezec, H. J.; Ghaemi, H. F.; Thio, T.; Wolff, P. A. Extraordinary Optical Transmission through Subwavelength Hole Arrays. *Nature* **1998**, *391*, 667–669.
15. Braun, J.; Gompf, B.; Kobiela, G.; Dressel, M. How Holes Can Obscure the View: Suppressed Transmission through an Ultrathin Metal Film by a Subwavelength Hole Array. *Phys. Rev. Lett.* **2009**, *103*, 203901.
16. Yokogawa, S.; Burgos, S. P.; Atwater, H. A. Plasmonic Color Filters for CMOS Image Sensor Applications. *Nano Lett.* **2012**, *12*, 4349–4354.
17. Burgos, S. P.; Yokogawa, S.; Atwater, H. A. Color Imaging *via* Nearest Neighbor Hole Coupling in Plasmonic Color Filters Integrated onto a Complementary Metal-Oxide Semiconductor Image Sensor. *ACS Nano* **2013**, *7*, 10038–10047.
18. Mansuripur, M.; Zakharian, A.; Lesuffleur, A. R.; Oh, S. H.; Jones, R. J.; Lindquist, N. C.; Im, H.; Kobyakov, A.; Moloney, J. V. Plasmonic Nano-structures for Optical Data Storage. *Opt. Express* **2009**, *17*, 14001–14014.
19. Yanik, A. A.; Huang, M.; Artar, A.; Chang, T. Y.; Altug, H. Integrated Nanoplasmonic-Nanofluidic Biosensors with Targeted Delivery of Analytes. *Appl. Phys. Lett.* **2010**, *96*, 021101.
20. Langguth, L.; Punj, D.; Wenger, J.; Koenderink, A. F. Plasmonic Band Structure Controls Single Molecule Fluorescence. *ACS Nano* **2013**, *7*, 8840–8848.
21. Jonsson, M. P.; Dekker, C. Plasmonic Nanopore for Electrical Profiling of Optical Intensity Landscapes. *Nano Lett.* **2013**, *13*, 1029–1033.
22. Rotenberg, N.; Krijger, T. L.; le Feber, B.; García de Abajo, F. J.; Kuipers, L. Magnetic and Electric Response of Single Subwavelength Holes. *Phys. Rev. B* **2013**, *88*, 241408.
23. Wang, T.; Boer-Duchemin, E.; Comtet, G.; Le Moal, E.; Dujardin, G.; Drezet, A.; Huant, S. Plasmon Scattering from Holes: From Single Hole Scattering to Young's Experiment. *Nanotechnology* **2014**, *25*, 125202.
24. Sigle, W.; Nelayah, J.; Koch, C. T. Electron Energy Losses in Ag Nanoholes—From Localized Surface Plasmon Resonances to Rings of Fire. *Opt. Lett.* **2009**, *34*, 2150–2152.
25. Prangsma, J. C.; van Oosten, D.; Kuipers, L. Local Investigation of the Optical Properties of Subwavelength Rectangular Holes with a Focused Beam of Electrons. *Philos. Trans. R. Soc. A* **2011**, *369*, 3456–3471.
26. von Cube, F.; Irsen, J.; Niegemann, S.; Matyssek, C.; Hergert, W.; Busch, K.; Linden, S. Spatio-Spectral Characterization of Photonic Meta-Atoms with Electron Energy-Loss Spectroscopy. *Opt. Mater. Epress* **2011**, *5*, 1009–1018.
27. Kuttge, M.; Vesseur, E. J. R.; Koenderink, A. F.; Lezec, H. J.; Atwater, H. A.; García de Abajo, F. J.; Polman, A. Local Density of States, Spectrum, and Far-Field Interference of Surface Plasmon Polaritons Probed by Cathodoluminescence. *Phys. Rev. B* **2009**, *79*, 113405.
28. Coenen, T.; Bernal Arango, F.; Koenderink, A. F.; Polman, A. Directional Emission from a Single Plasmonic Scatterer. *Nat. Commun.* **2014**, *5*, 3250.
29. van Wijngaarden, J. T.; Verhagen, E.; Polman, A.; Ross, C. E.; Lezec, H. J.; Atwater, H. A. Direct Imaging of Propagation and Damping of Near-Resonance Surface Plasmon Polaritons Using Cathodoluminescence Spectroscopy. *Appl. Phys. Lett.* **2006**, *88*, 221111.
30. FDTD Solutions; Lumerical Solutions Inc.; www.lumerical.com.
31. Lezec, H. J.; Degiron, A.; Devaux, E.; Linke, R. A.; Martín-Moreno, L.; Garcia-Vidal, F. J.; Ebbesen, T. W. Beaming Light from a Subwavelength Aperture. *Science* **2002**, *297*, 820–822.

32. López-Tejeira, F.; Rodrigo, S. G.; Martín-Moreno, L.; García-Vidal, F. J.; Devaux, E.; Ebbesen, T. W.; Krenn, J. R.; Radko, I. P.; Bozhevolnyi, S. I.; González, M. U.; *et al.* Efficient Unidirectional Nanoslit Couplers for Surface Plasmons. *Nat. Phys.* **2007**, *3*, 324–328.
33. Aouani, H.; Mahboub, O.; Bonod, N.; Devaux, E.; Popov, E.; Rigneault, H.; Ebbesen, T. W.; Wenger, J. Bright Unidirectional Fluorescence Emission of Molecules in a Nanoaperture with Plasmonic Corrugations. *Nano Lett.* **2011**, *11*, 637–644.
34. Jun, Y. C.; Huang, K. C. Y.; Brongersma, M. L. Plasmonic Beaming and Active Control over Fluorescent Emission. *Nat. Commun.* **2011**, *2*, 283.
35. Kerker, M.; Wang, D. S.; Giles, C. L. Electromagnetic Scattering by Magnetic Spheres. *J. Opt. Soc. Am.* **1983**, *73*, 765–767.
36. Lee, S. Y.; Lee, I. M.; Park, J.; Oh, S.; Lee, W.; Kim, K. Y.; Lee, B. Role of Magnetic Induction Currents in Nanoslit Excitation of Surface Plasmon Polaritons. *Phys. Rev. Lett.* **2012**, *108*, 213907.
37. Coenen, T.; Vesseur, E. J. R.; Polman, A. Angle-Resolved Cathodoluminescence Spectroscopy. *Appl. Phys. Lett.* **2011**, *99*, 143103.
38. Fu, Y. H.; Kuznetsov, A. I.; Miroshnichenko, A. E.; Yu, Y. F.; Luk'yanchuk, B. Directional Visible Light Scattering by Silicon Nanoparticles. *Nat. Commun.* **2013**, *4*, 1527.
39. Person, S.; Jain, M.; Lapin, Z.; Sáenz, J. J.; Wicks, G.; Novotny, L. Demonstration of Zero Optical Backscattering from Single Nanoparticles. *Nano Lett.* **2013**, *13*, 1806–1809.
40. Staude, I.; Miroshnichenko, A. E.; Decker, M.; Fofang, N. T.; Liu, S.; Gonzales, E.; Dominguez, J.; Luk, T. S.; Neshev, D. N.; Brener, I.; *et al.* Tailoring Directional Scattering through Magnetic and Electric Resonances in Subwavelength Silicon Nanodisks. *ACS Nano* **2013**, *7*, 7824–7832.
41. van de Groep, J.; Polman, A. Designing Dielectric Resonators on Substrates: Combining Magnetic and Electric Resonances. *Opt. Express* **2013**, *21*, 26285–26302.
42. Bernal Arango, F.; Coenen, T.; Koenderink, A. F. Underpinning Hybridization Intuition for Complex Antennas by Magnetoelectric Quadrupolar Polarizability Retrieval. *ACS Photonics* **2014**, *1*, 444–453.
43. Logeeswaran, V. J.; Kobayashi, N. P.; Islam, M. S.; Wu, W.; Chaturvedi, P.; Fang, N. X.; Wang, S. Y.; Williams, R. S. Ultrasmooth Silver Thin Films Deposited with a Germanium Nucleation Layer. *Nano Lett.* **2009**, *9*, 178–182.
44. Liu, H.; Wang, B.; Leong, E. S. P.; Yang, P.; Zong, Y.; Si, G.; Teng, J.; Maier, S. A. Enhanced Surface Plasmon Resonance on a Smooth Silver Film with a Seed Growth Layer. *ACS Nano* **2010**, *4*, 3139–3146.
45. Coenen, T.; Vesseur, E. J. R.; Polman, A.; Koenderink, A. F. Directional Emission from Plasmonic Yagi Uda Antennas Probed by Angle-Resolved Cathodoluminescence Spectroscopy. *Nano Lett.* **2011**, *11*, 3779–3784.
46. Palik, E. D. *Handbook of Optical Constants*; Academic Press: New York, 1985.
47. Johnson, P. B.; Christy, R. W. Optical Constants of the Noble Metals. *Phys. Rev. B* **1972**, *6*, 4370–4379.